Carbon 185 (2021) 395–403

Contents lists available at ScienceDirect

Carbon

journal homepage: www.elsevier.com/locate/carbon

Research Paper

Functional group tuning of two-dimensional carbon nanosheets for boosting oxygen reduction electrocatalysis

Gao Li [a, 1], Huanhuan Guo [b, 1], Zeming Wang [a, 1], Hong Bao [a], Guanhui Gao [c], Bingjie Hu [a], Lijie Ci [d], Liang Wang [a, *], Minghong Wu [e, f, **]

[a] Institute of Nanochemistry and Nanobiology, School of Environmental and Chemical Engineering, Shanghai University, 99 Shangda Road, BaoShan District, Shanghai, 200444, PR China
[b] Key Laboratory for Liquid-Solid Structural Evolution & Processing of Materials (Ministry of Education), Research Center for Carbon Nanomaterials, School of Materials Science and Engineering, Shandong University, 17923 Jingshi Road, Jinan, 250061, PR China
[c] Department of Materials Science and NanoEngineering, Rice University, 6100 Main Street, Houston, TX, 77005, USA
[d] School of Materials Science and Engineering, Harbin Institute of Technology, Shenzhen University Town, Nanshan District, Shenzhen, 518055, PR China
[e] Shanghai Institute of Applied Radiation, Shanghai University, 99 Shangda Road, BaoShan District, Shanghai, 200444, PR China
[f] Key Laboratory of Organic Compound Pollution Control Engineering (MOE), Shanghai University, 99 Shangda Road, BaoShan District, Shanghai, 200444, PR China

ARTICLE INFO

Article history:
Received 20 May 2021
Received in revised form
23 August 2021
Accepted 17 September 2021
Available online 21 September 2021

Keywords:
Carbon nanosheets
Sterculia lychnophora
Functional group
Freeze-drying
Oxygen reduction reaction

ABSTRACT

The N-doped carbon materials have natural advantages as the potential catalyst of oxygen reduction reaction (ORR). However, the lack of practical synthesis techniques for enabling highly efficient ORR performance hinders the go-ahead of robust carbocatalysts. Here, we design and synthesize nitrogen-doped carbon nanosheets (N–CN-Fd) with abundant activate sites from Sterculia lychnophora via a brief freeze-drying technology. This universal route promotes the specific surface areas, strengthens the degree of graphitization and increases the atom ratio of electron-donating groups of N–CN-Fd. The obtained N–CN-Fd displays an onset potential of 0.91 V, a half-wave potential of 0.79 V, and a limited-diffusion current density of 3.6 mA/cm^2 for ORR under alkaline conditions, comparable to commercial Pt/C. Meanwhile, a four-electron ORR pathway is revealed and N–CN-Fd maintains higher stability than Pt/C in chronoamperometric response. Moreover, the advantage of the N–CN-Fd catalyst in increasing the discharge-charge capacity and improving the cycling stability of the Li–O_2 battery is demonstrated. The theoretical calculation result illustrates that the abundant electron-donating surface groups on the samples able to accomplish the activation of ortho-C atoms, which endow N–CN-Fd the excellent ORR activity. Our findings provide guidelines for designing various carbon-based electrocatalysts with multiple active sites through freeze-drying crafts.

1. Introduction

Exploiting green and renewable energy is one of the practical approaches to promote sustainable development [1,2]. Oxygen reduction reaction (ORR) plays a vital role in engineering the performance of devices, such as metal-air batteries and fuel cells [2–6]. However, the overall efficiency of these devices has been inhibited by the slack kinetics in the ORR process [7,8]. Therefore, traditional noble metal-containing Pt and its alloys have been extensively used as electrocatalysts with high ORR activity [9–11]. Unfortunately, they are still plagued with problems that restrict their practical applications of these renewable energy devices [12–14], such as the exorbitant price, scarcity in nature, and easy deactivation. To address these inherent challenges, ORR electrocatalysts have been investigated to perform a highly efficient, friendly environment and low-cost [15].

Among these researched materials, carbon nanomaterials as metal-free electrocatalysts are one of the best choices to satisfy the aforementioned conditions for storing and converting energy due to their abundant, adjustable morphology and ease of

* Corresponding author.
** Corresponding author. Shanghai Institute of Applied Radiation, Shanghai University, 99 Shangda Road, BaoShan District, Shanghai, 200444, PR China.
E-mail addresses: wangl@shu.edu.cn, wanglcarbon@vip.163.com (L. Wang).
[1] These authors contributed equally: G. Li, H. Guo, Z. Wang.

https://doi.org/10.1016/j.carbon.2021.09.042
0008-6223/

functionalization [16,17]. The inherent challenge in pure carbon materials is the shortage of sufficient active sites despite their good electrical conductivity. The carbon nanomaterials' electrocatalytic performance can be strengthened through their nanoarchitecture engineering, heteroatom doping, and surface functionalization [10,18–20]. These regulation strategies provide a prospective way to break the blocking effect to obtain a high density of active sites [21], then the carbon nanomaterials can work as excellent building blocks for high ORR performance [22–24].

The electron-donating/withdrawing groups on the edge/surface of carbon materials, such as NH_2-, COOH-, OH-, and types of N-doping are certificated to be indispensable for widely tuning ORR activity and optimizing active sites [6,25–27]. However, to date, the nature of the active sites between electron-donating groups and electron-withdrawing groups is still controversial. More importantly, the lack of presently practical synthesis techniques hinders the go-ahead of robust carbocatalysts [28]. Supposing carbocatalysts synthesized by existing mature technologies can address the above controversy and elucidate the role of relative functional groups, there is a most satisfactory way to gain a principle understanding for the synthesis of carbon-based catalysts [13,29], which affects the development of late-model catalytic materials with magnanimous of active sites by electron-donating/withdrawing group engineering [6].

Here, we elaborately develop a two-dimensional (2D) graphene-like nitrogen-doped carbon nanosheets (N–CN-Fd) catalyst from Sterculia lychnophora (Sl) via a commercial freeze-drying technology. This universal route promotes the specific surface areas, strengthens the degree of graphitization and increases the atom ratio of electron-donating groups of N–CN-Fd. Moreover, as-synthesized samples are demonstrated as a stable four-electron transfer pathway after tested and could be a suitable ORR catalyst as an air electrode for Li–O_2 battery. Notably, the engineering mission of freeze-drying technology in the synthesis process of catalysts is investigated powerfully, combining first-principles calculation with experimental data. Using common processing techniques, our strategy helps to accurately engineer functional electron-donating/withdrawing groups and provides a theoretical foundation for the design of carbon-based catalysts.

2. Experimental section

2.1. Synthesis of N–CN-Fd and other control samples

Typically, a mixture of raw material Sl and melamine (Mel) with a mass ratio of 1:1 was first placed into a 100 mL beaker, 50 mL of deionized water was added and stirred 2 h at 80 °C. Subsequently, freeze-drying was applied to the mixture for 48 h to obtain the solid product called Sl-Mel-Fd (SCIENTZ-12ND, Ningbo Scientz Biotechnology Co., Ltd., Ningbo, China.www.scientz.com). Then, the powder of Sl-Mel-Fd was pyrolyzed and carbonized at 900 °C for 2 h under an N_2 atmosphere. After washing with deionized water and ethanol, N–CN-Fd was obtained. For the synthesis of N–CN-Fd-(800 and 1000), they were similarly treated by the process of N–CN-Fd and except for carbonized at 800 and 1000 °C, respectively. For the synthesis of N–CN-Fd-(1:2 and 2:1), they were similarly treated by the process of N–CN-Fd and except for a mass ratio of 1:2 and 2:1 between Sl and melamine, respectively. For the synthesis of CN, the Sl precursor was carbonized directly. For the synthesis of Sl-Mel-Nfd, the mixture of Sl and melamine was directly dried at 80 °C for 12 h. Then, the Sl-Mel-Nfd was pyrolyzed and carbonized at 900 °C for 2 h under an N_2 atmosphere, and the N–CN-Nfd was finally produced.

2.2. Material characterization

Analysis of sample morphologies was performed on a scanning electron microscope (SEM, JEOL JSM-6490) and Scanning/Transmission Electron Microscope (FEI Titan 80–300) with an energy dispersion spectrum (EDS). Nitrogen sorption/desorption measurements (JW-BK100A) were applied to analyze the change of pore size and Brunauer-Emmett-Teller (BET) surface area of samples. The crystallization phase identification is employed by X-ray diffraction (XRD, Rigaku D/max-2500). Functional groups on the surface of samples were characterized by Fourier transform adsorption spectrum (FTIR, FTS165) and X-ray photoelectron spectroscopy (XPS, Thermo Fischer, ESCALAB250Xi). The Raman spectra information is also given in DXRxi excitation with a 633 nm laser. The galvanostatic discharge-charge cycling tests of Li–O_2 batteries were performed on a Land CT2001A system at a current density of 50 mA g^{-1} (catalyst).

2.3. Electrochemical characterization

CHI760E electrochemical workstation (Shanghai Chenhua Instruments Co., China) took on the work of electrochemical characterization. The test was performed under a three-electrode system, in which a glassy carbon electrode, a graphite electrode, and an Ag/AgCl/3 M KCl electrode were used as the working, auxiliary, and reference electrodes, respectively. For a typical working electrode, the mixture with 5 mg of the as-synthesized sample, 250 μL of isopropanol, 700 μL of DI water, and 50 μL of Nafion solution was sonicated for 60 min. Then, 10 μL ink with good dispersibility was coated evenly on the glassy carbon disk and dried naturally at room temperature. And the mass loading of catalysts on the working electrode was about 0.25 mg cm^{-2}. The electrochemical properties of commercial 20 wt% Pt/C catalysts were also tested for comparison.

Characterization test on ORR, 0.1 M KOH solution was acted as the alkaline medium, respectively, and were saturated with N_2/O_2 for not less than 30 min before the electrochemical characterization was performed. CV curves were obtained in N_2/O_2 saturated electrolyte solutions at a scan rate of 50 mV s^{-1}. LSV scanning in N_2/O_2 saturated electrolyte, the scan rate set to 10 mV s^{-1}, and the rotating speed of the Rotating Disc Electrode (RDE) is 1600 rpm. The long-term stability was investigated by chronoamperometric after 10 h at 0.67 V and 1600 rpm. Besides, the K-L equation plays a role in calculating the number of transferred electrons, and the equations as follows:

$$J^{-1} = J_L^{-1} + J_K^{-1} = (B\omega^{2/3}) + J_K^{-1} \quad (1)$$

$$B = 0.62nFC_oD^{2/3}\nu^{-1/6} \quad (2)$$

Wherein, J is the current density that can be obtained in the experimental results, n represents the number of electrons transferred, J_L and J_K refer to the diffusion-limiting current density and kinetic current density, ω is the electrode rotating rate, F is Faraday constant (96485 C/mol), The bulk concentration of O_2 in 0.1 M KOH (1.2×10^{-3} mol/L) is expressed in C_0, the diffusion coefficient of O_2 in 0.1 M KOH (1.9×10^{-5} cm^2/s) is expressed in D, the viscosity of the electrolyte (0.01 cm^2/s) is expressed in ν.

The H_2O_2 yield was monitored through an RRDE with a Pt ring set at 1.2 V (collection factor is 24.9%) and a catalyst-coated GC disk (the effective area is 19.63 mm^2). during ORR and further evaluated the n. The formulas for calculating the hydrogen peroxide yield of different catalysts are as follows [30]:

$$H_2O_2 = 200*\frac{\frac{I_R}{N}}{\frac{I_R}{N} + I_D} \quad (3)$$

$$n = 4*\frac{I_D}{\frac{I_R}{N} + I_D}. \quad (4)$$

where I_R and I_D correspond to the ring and disk currents, respectively.

2.4. Theoretical calculations

The spin-polarized periodic DFT calculations of electrocatalytic active sites and energies in vacuum were performed using Vienna ab-initio simulation package (5.4.4 VASP) [31] with the projector augmented-wave method (PAW) [32], in addition, the convergence criteria of 10^{-4} eV in electronic relaxation and 0.02 eV/Å in force with conjugate-gradient algorithm were adopted. The Perdew-Burke-Ernzerhof (PBE) functional within generalized gradient approximation (GGA) [33] was employed. The plane-wave cutoff energy was set to 450 eV. The Brillouin zone of the periodic 2D slab separated with a 15 Å vacuum space along the Z-axis was sampled with $2 \times 2 \times 1$ and $4 \times 4 \times 1$ k-points grids for geometry optimization and electronic structure calculations, respectively [34]. The unit cell size is set at 20×20 Å to avoid interactions between the imaging cells. Fermi-smearing of $k_BT = 0.1$ eV was employed to speed up the convergence. And the solvation (water) effect is evaluated by an implicit solvation model implemented in the VASPsol code, which accounts for the effects of electrostatics, cavitation, and dispersion on the interaction between a solute and solvent into the plane-wave DFT code VASP [35,36], in the simulated water environment, the final optimal structure is based on the relaxation results in a vacuum until the convergence standard. Data handling of free energy calculations and reaction mechanism was shown in supporting information.

2.5. Li–O_2 battery assembling

The galvanostatic discharge-charge cycling tests of Li–O_2 batteries were performed on a Land CT2001A system at a current density of 50 mA $g^{-1}_{(catalyst)}$. Different catalysts materials (N–CN-Fd and CN) were mixed with super P and PVDF (6:3:1, w/w) and dispersed in the NMP solution to obtain a uniform mixture. The air electrodes were prepared by coating the above mixture on the porous carbon paper. The mass loading of active material on an air electrode is about 0.60 mg after drying. The Li–O_2 cells were assembled with an air electrode, 100 μL tetramethylene glycol dimethyl ether (TEGDME) containing 1 M LiTFSI salt, and a Li metal anode in an Ar-filled glove box ($H_2O \leq 0.1$ ppm, $O_2 \leq 0.1$ ppm). All the cells were kept in a sealed O_2-filled bottle (1 atm) for 6 h before cycling.

3. Results and discussion

3.1. Synthesis and structure characterization

Converting biomass waste into carbon-based materials is an economical and renewable pathway to achieve high value-added products easily. Sterculia lychnophora (Sl) is a joint plant with the function of moistening the lung and detoxifying in our daily life. While immersing Sl in boiling water, Sl swells greatly and then forms a brown porous Jellyfish-like sponge with wonderful layers. Above this manifest phenomenon, the N–CN-Fd is first synthesized from Sl (Fig. 1a). A precursor solution is first prepared by dissolving Sl and melamine in hot water. Then, a traditional freeze-drying technic coupled with calcination is applied to treat the mixture and finally obtain N–CN-Fd. The optimum pyrolysis temperature and a mass ratio of raw material (Sl and melamine) was 900 °C and 1:1 according to the electrocatalysis performance of the samples, respectively (Fig. S1). To investigate the role of freeze-drying technology in the synthesis process, the control samples are synthesized, whose detailed preparation procedures are described in the experimental section. Initially, melamine vaporizes quickly at low temperatures in the freeze-drying process (Fig. S2), causing a lower N content of Sl-Mel-Fd than that of Sl-Mel-Nfd, as evidenced in Fig. S3 and Table S1. Meanwhile, a noticeable increase of oxygen content of Sl-Mel-Fd has illustrated in the X-ray photoelectron spectroscopic (XPS) results (Fig. S3 and Table S1), resulting from the formation of more oxygen-containing functional groups on Sl-Mel-Fd during the freeze-drying process (Table S1). Furthermore, an improved surface area of Sl-Mel-Fd is presented in Fig. S4, which is about 1.4-fold than drying Sl-Mel-Nfd. Thus, melamine has the effects of "one stone, two birds", acting as both an N source and a porogen to generate pores in the freeze-drying process. The freeze-drying technology has been proven to act a unique and crucial role in controlling the morphology and structure of Sl-Mel-Fd (Fig. S5), which in turn affects the properties of the carbonized N–CN-Fd.

To examine the morphology of N–CN-Fd, transmission electron microscopy (TEM) is performed. The TEM imaging in Fig. 2a reveals that the N–CN-Fd has a similar morphologic feature to graphene with a sheet-like architecture. The color of the samples between CN to N–CN-Fd turns from grey-black to light grey, signifying the variation of the thickness (Figs. S6–S8). The width of the nanosheets is estimated at 2 μm (typically 1 μm) in TEM, whereas the height measured by atomic force microscopy (AFM) is approximately 4 nm, equivalent to twelve or fewer graphene layers (Fig. 2b and Fig. S9). The scanning electron microscopy (SEM) image (Fig. 2c) shows mainly a nanoporous structure constructing with graphene-like nanoflakes, coordinating with TEM and AFM results. Furthermore, the element mapping images (Fig. 2d) illustrate the uniform distribution of C, N, and O elements throughout the N–CN-Fd, indicating that the N atoms are well dispersed on N–CN-Fd via freezing-dry. Combining with the SEM of compared samples in Figs. S10–11, the morphology of as-prepared samples has changed from nonporous bulk material to a thin graphene-like nanosheet constructed porous nanomaterial ranging from CN to N–CN-Fd, which is further verified by their specific surface area (Fig. 2e and Fig. S12). The characterized specific surface area of the N–CN-Fd is ~238.2 m^2/g, significantly more extensive than that of the CN (~4.3 m^2/g) and the N–CN-Nfd (~9.7 m^2/g). The pore size distribution of N–CN-Fd (insert in Fig. 2e and Fig. S12c) exhibits a multilevel porous structure, containing 17.4% macropores for material transport and 82.6% mesopores for the diffusion of reactants and products. Furthermore, the high porosity of ~0.2 $cm^3\ g^{-1}$ also guarantees abundant active sites on the edge and surface of N–CN-Fd by freeze-drying technology.

XRD pattern (Fig. S13) is carried out to reveal the crystalline structure. All the samples display a (002) layer spacing, which is similar to that of bulk graphite at 3.34 Å. Among them, the CN has a broad peak with an interlayer spacing of 3.66 Å. In opposite, N–CN-Fd shows the decreasing interlayer spacing from 3.66 to 3.51 Å, illustrating the freeze-drying treatment can reduce the interlayer spacing of samples due to the transition from crystalline CN to amorphous N–CN-Fd. Detailed information on the defects of the prepared materials is obtained to utilize the Raman spectra. As presented in Fig. S14, the intensity of the typical ordered G band appears at 1681 cm^{-1} is more robust than that of the disordered D band identifies at 1331 cm^{-1} in all the samples. However, the D to G intensity ratio decreases gradually from CN to N–CN-Fd. These

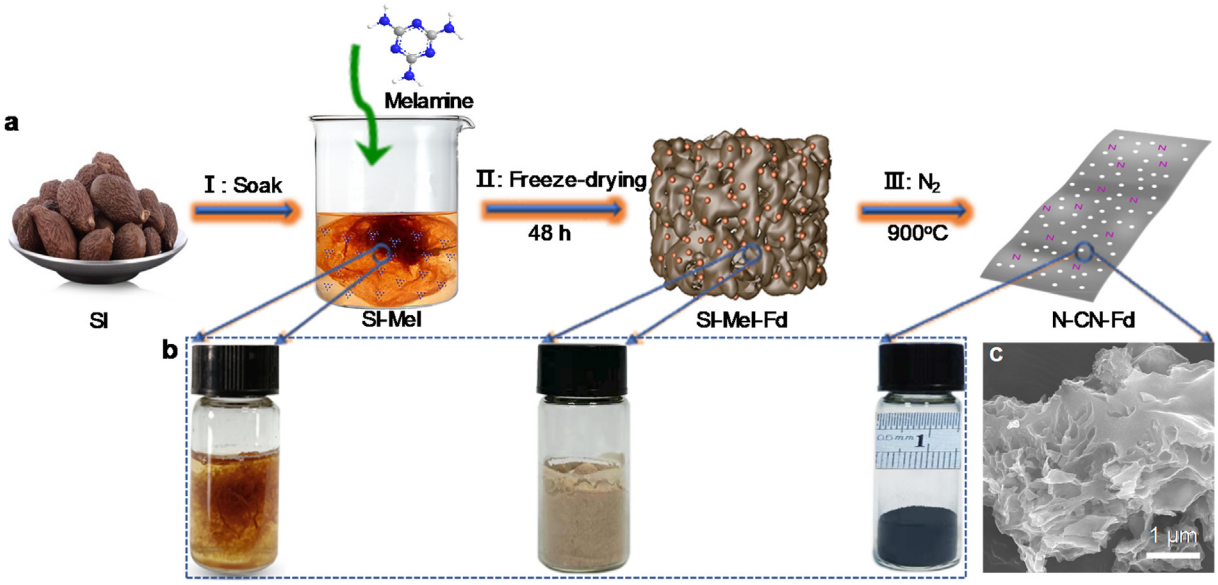

Fig. 1. (a) Synthesis steps: I mixing Sl and melamine in hot water, II freeze-drying for 48 h, and III carbonization at 900 °C for 2 h. (b) The images of the samples. (c) The TEM image of N–CN-Fd. (A colour version of this figure can be viewed online.)

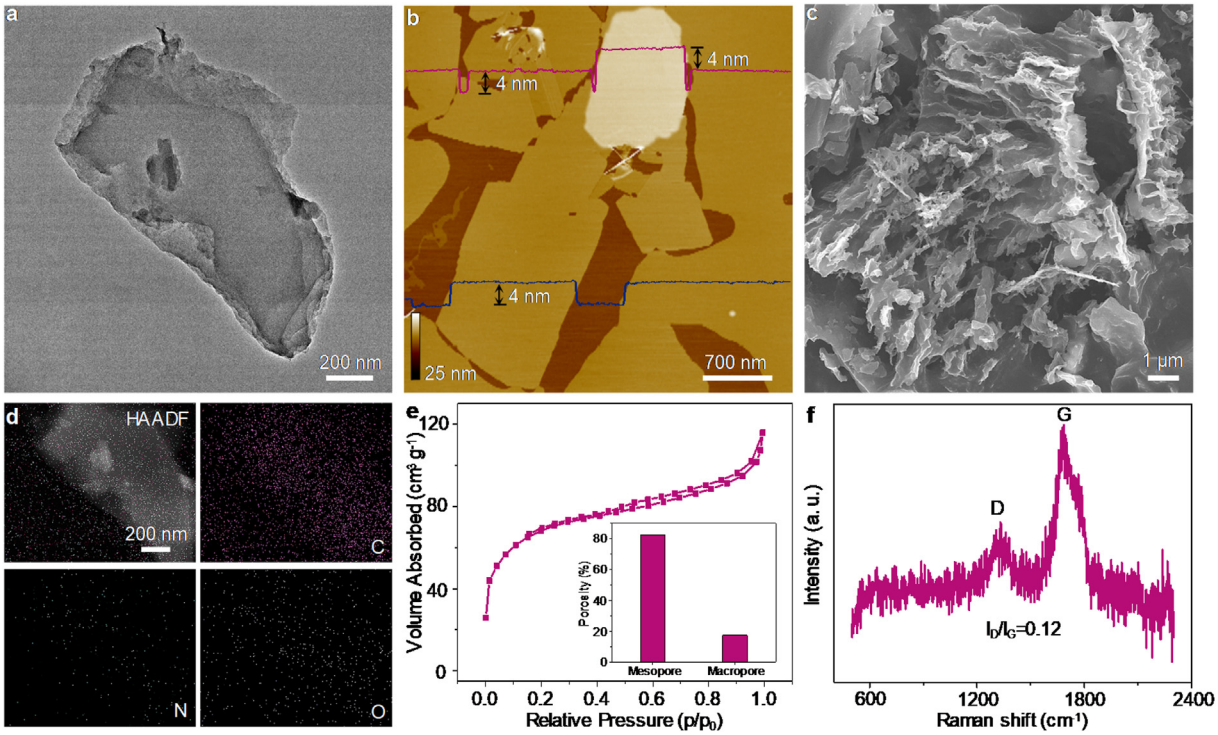

Fig. 2. (a) TEM image of N–CN-Fd. (b) AFM image and height profile of the N–CN-Fd on a mica substrate. (c) SEM image of N–CN-Fd. (d) SEM image and corresponding elemental mapping images of N–CN-Fd. (e) N_2 sorption isotherms and BET pore size distribution of N–CN-Fd. (f) Raman spectrum of N–CN-Fd. (A colour version of this figure can be viewed online.)

results confirm the evolution of N–CN-Fd from CN with improving graphitization degree by eliminating some defects, which indicates an enhanced conductivity and improved electrocatalytic performance of N–CN-Fd as an electrocatalyst.

Typically, Fourier-transform IR (FT-IR) and XPS characterization technology layout the chemical composition and functional groups of the surface of as-synthesized catalysts. For the FT-IR spectra (Fig. 3a), the species of the surface functional groups of the three samples are not varied. The narrow peaks at 1038, 1145, 1550, 1743, 2120, 2320, and 2667 cm^{-1} are related to the stretching vibration peaks of C–N, C–OH, C–C, C=O, C=C, N–H, and O–H, respectively. Besides, the content varieties of surface functional groups of samples are further analyzed by XPS. As shown in Fig. 4b and Table S2, the XPS survey spectra give the three distinct peaks are C1s, N1s, and O1s, and the binding energy is 284.60, 399.10, and 531.10 eV, respectively. Among them, the C content of N–CN-Fd is estimated

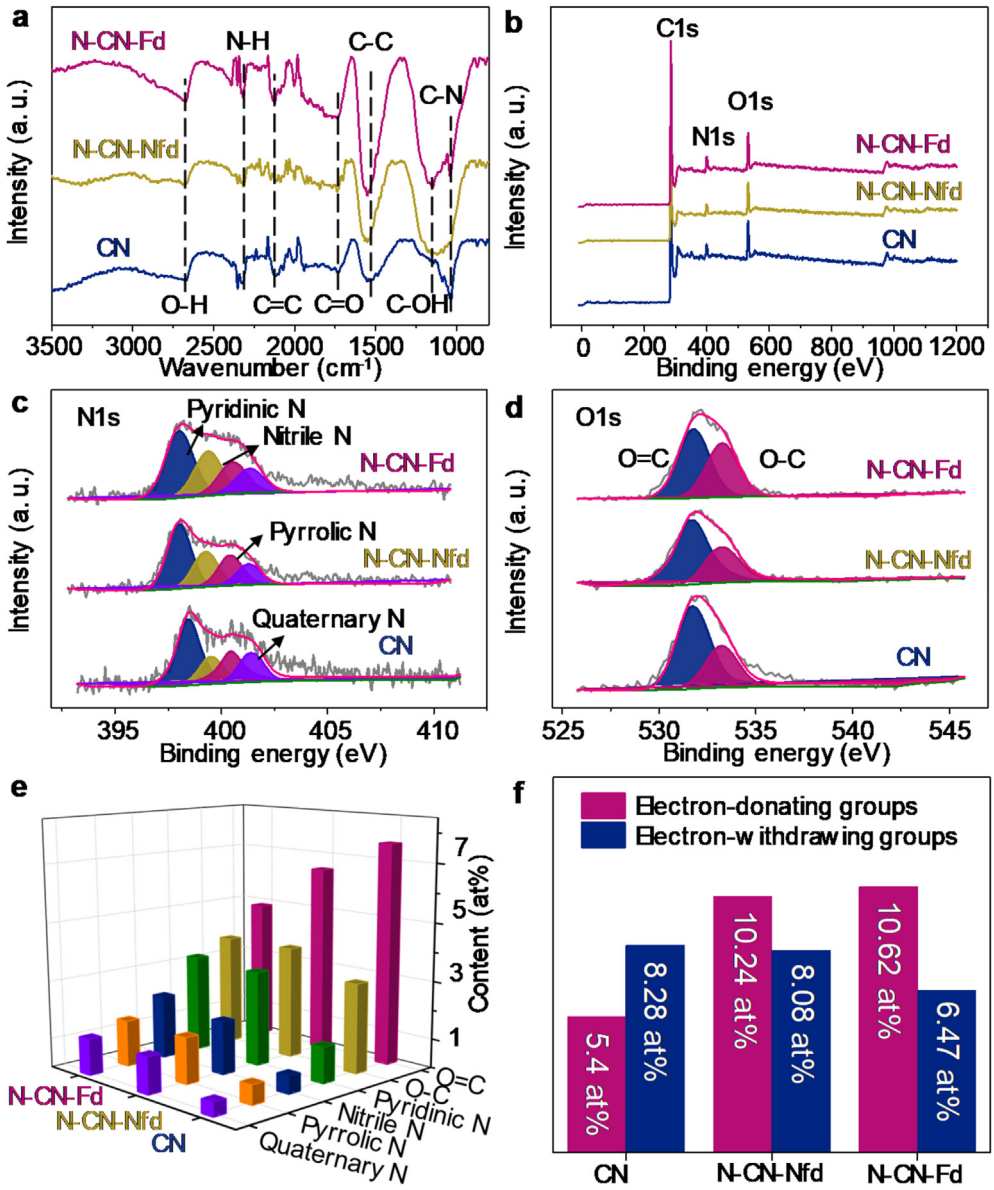

Fig. 3. (a) FT-IR spectra of N–CN-Fd, N–CN-Nfd, and CN. (b) XPS survey spectra, high-resolution XPS N1s (c) and O1s (d) spectra of N–CN-Fd, N–CN-Nfd, and CN. (e) Surface group content of N–CN-Fd, N–CN-Nfd, and CN. (f) Histogram of the content distribution of electron-withdrawing groups and electron-donating groups. (A colour version of this figure can be viewed online.)

to be as similar as that of N–CN-Nfd. Then, the O content of N–CN-Fd decreases from 10.4 to 8.7 at% after freeze-drying treatment whereas their N content of N–CN-Fd increases from 3 to 8.4 at%, which demonstrated abundant N element doped into the N–CN-Fd successfully. Based on the above results and Fig. 3c and e analysis, four different types of N are likely to combine with the carbon skeleton of the samples, including pyridinic N, nitrile N, pyrrolic N, and quaternary N, and the binding energies are 398.01, 399.38, 400.53, 401.33 eV, respectively. These N groups have a similar growing trend ranging from CN to N–CN-Fd. Different from the hardly change phenomenon of pyridinic/pyrrolic N content between N–CN-Nfd and N–CN-Fd, the quaternary N content increases from 1.09 to 1.22 at% in the transition from N–CN-Nfd to N–CN-Fd, which is corresponding with the Raman results. The electron-donating quaternary N in the samples provides electrons to the π-connected system and enhances oxygen adsorption, attributed to the increase of nucleophilic interaction between carbon rings, which will enhance the ORR activity. On the other hand, quaternary N can inhibit the adsorption of water oxidation intermediate (OH^- and OOH^-) by its nearby C atom in alkaline conditions and are thereby favorable for ORR. Similarly, the electron-donating nitrile content also increases from 1.89 to 2.2 at% ranging from N–CN-Nfd to N–CN-Fd, supposing that the electron-donating groups on the surface of N–CN-Fd are mainly active sites in the ORR process. Furthermore, the decreasing trending of electron-withdrawing O=C signals in the high-resolution O1s spectra (Fig. 3d and e, and Table S2) further verify our previous hypothesis. Overall, as shown in Fig. 3f, the total ratio of the electron-withdrawing groups of the three samples decreases whereas the total amount of electron-donating groups increases ranging from CN to N–CN-Fd, supposing the electron-donating groups of the catalyst is the governing active sites to boost the ORR process.

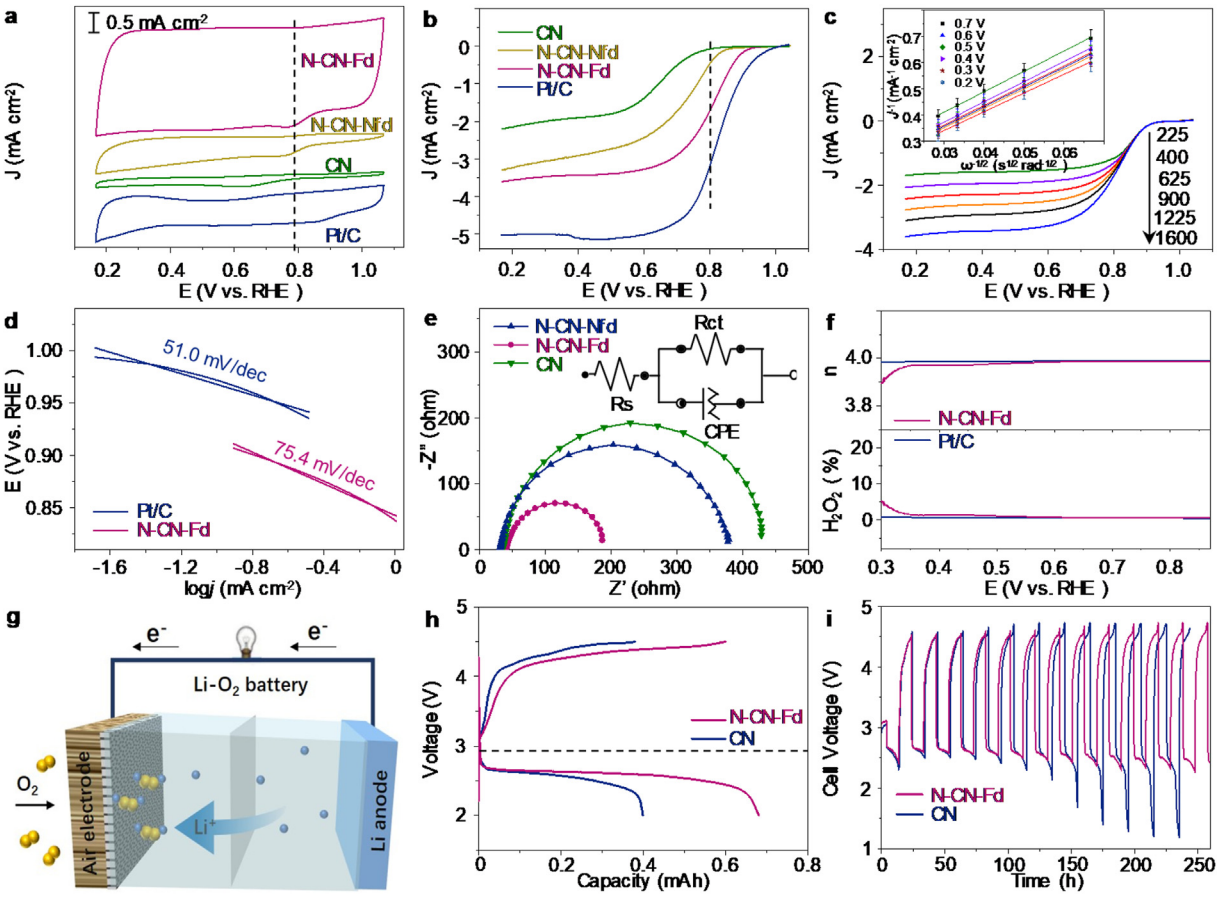

Fig. 4. (a) CV curves of N–CN-Fd, N–CN-Nfd, and CN in O_2-saturated 0.1 M KOH solutions without rotation at 25 °C. (b) LSV curves of N–CN-Fd, N–CN-Nfd, and CN in the O_2-saturated 0.1 M KOH with a scan rate of 10 mV s^{-1} at a rotating rate of 1600 rpm at 25 °C. (c) LSV curves of N–CN-Fd at different rotation rates. Inset: K-L plots. (d) The corresponding Tafel Plots. (e) Nyquist plots for N–CN-Fd, N–CN-Nfd, and CN. Z′ and Z" are the real and imaginary parts of the impedance. Inset: Equivalent circuit diagram for impedance spectra data fitting. (f) Electron-transfer number (top) and hydrogen peroxide yield (bottom) of N–CN-Fd and Pt/C. (g) Schematic of the rechargeable Li–O_2 battery. (h) Galvanostatic discharge-charge curves of Li–O_2 batteries at the current density of 50 mA g^{-1} (catalyst). The initial deep discharge-charge curves of Li–O_2 batteries from 2.0 V to 4.5 V. (i) The cycling curves of Li–O_2 batteries with a limited capacity of 500 mAh g^{-1} (catalyst). (A colour version of this figure can be viewed online.)

3.2. ORR and Li–O_2 battery performance of the N–CN-Fd catalyst

The ORR catalytic performance of the as-obtained electrocatalyst and commercial Pt/C (20%) used as the control catalyst is evaluated in 0.1 M KOH electrolyte. The most positive reduction peak potential (E_p) of N–CN-Fd at 0.79 V is noticed in the cyclic voltammetry (CV) curves (Fig. 4a) and is close to the value approach of Pt/C (0.8 V), which implies its superior ORR electrocatalytic activity. The linear scan voltammogram (LSV) curves (Fig. 4b and c) contribute to confirm the outstanding ORR achievement of N–CN-Fd. The results reveal that the N–CN-Fd gave a superior ORR activity with an onset potential (E_{onset}) of 0.91 V and half-wave potential ($E_{1/2}$) of 0.79 V vs. RHE, only less negative than that of Pt/C (0.82 V). The limiting current density (J_L) of 3.6 mA cm^{-2} and superior to other contrast materials [37,38]. According to LSV curves, when adding the technology of freeze-drying and N-doping into the process of catalysts, the E_{onset}, $E_{1/2}$ increase obviously (Table S3). Fig. 4c displays the LSV curves of N–CN-Fd at diverse rotation speeds in 0.1 M KOH saturated oxygen. The limiting current density of N–CN-Fd increases with rotating rates rising due to the decrease of spread distance and the increase of the rotating speed. The Koutecky–Levich (K-L) equation is served to compute kinetic current density. The K-L curve shows good linearity, and has a homologous slope under different potential, indicating that N–CN-Fd presents a first-order reaction kinetics process in ORR, and has a similar transfer electron number within a certain potential range [39]. The number of transferred electrons (n) is computed to be about 3.8 from the slopes of the K-L plots at different potentials (inset in Fig. 4c), suggesting that N–CN-Fd favors a $4e^-$ electrode process [40–42]. The Tafel slope can reveal reaction dynamics as observed in Fig. 4d. The Tafel slope of 75.4 mV·dec^{-1} for N–CN-Fd is very close to that of Pt/C (51.0 mV·dec^{-1}), reveals that N–CN-Fd can efficiently prompt the reduction of oxygen at a relatively low overpotential. The excellent ORR activity of N–CN-Fd mainly originates from the introduction of electron-donating groups into N–CN-Fd. Furthermore, the addition of the electron-donating groups into N–CN-Fd does not sacrifice their electronic conductivity, verified by electrochemical impedance spectroscopy (EIS) measurements (Fig. 4e). The semicircle in Nyquist plots from EIS of N–CN-Fd is less than the other two comparative samples, and it can be known from the impedance spectra fitting results from the Nyquist diagram in Table S4 (inset in Fig. 4e) demonstrating that N–CN-Fd has a desirable electronic transmission capability. To further investigate the ORR pathways for the N–CN-Fd electrode, the measurement is carried out on a rotating ring-disk electrode (RRDE) (Fig. S15). Fig. 4f illustrates that the H_2O_2 yield of N–CN-Fd is less than 5%, besides the n ranges within 3.9–4.0 within the potential range of 0.3–0.9 V, which is very close to the value of Pt/C. These data show us a gratifying electron transfer efficiency and a four-electron ORR pathway. According to the above analysis, the

freeze-drying technology is worthwhile for ORR via increasing the electron-donating surface groups of N–CN as the robust active sites.

In the matter of application in energy conversion devices, catalysts require not only outstanding ORR catalytic capability but also satisfactory stability [16,43–46]. The N–CN-Fd electrode exhibits better long-term stability in oxygen-saturated 0.1 M KOH comparing with the Pt/C catalyst shown in Fig. S16. The current change of N–CN-Fd is relatively smaller compared with the initial current after 36000 s continuous potentiostatic current test in 0.1 M KOH, and the current retention rate of 80.4% is successfully achieved, while that of Pt/C is only 56.7%, which reveals that N–CN-Fd material demonstrates better stability than that of Pt/C.

With the excellent stability of the catalyst, Li–O_2 batteries are assembled to inspect the excellent performance of N–CN-Fd in Fig. 4g and h illustrates the galvanostatic voltage profiles during the initial in-depth discharge-charge process [47]. Li–O_2 cell with N–CN-Fd catalyst displays a higher discharge voltage plateau and lower charge voltage plateau than that of the CN catalyst, due to its high ORR performance. Moreover, the N–CN-Fd sample yields a large discharge capacity of 0.68 mAh till 2.0 V and a charge capacity of 0.60 mAh till 4.5 V. In contrast, the discharge voltage of the CN sample quickly decreases to the cutoff voltage (2.0 V). Meanwhile, we investigate the cycling performance under the fixed capacity of 500 mAh g^{-1} (catalyst). As demonstrated in Fig. 4i, the Li–O_2 cell with a CN catalyst only operates seven cycles before the terminal discharge voltage reaches 2.0 V. In comparison, the N–CN-Fd-based Li–O_2 battery cycles steadily over 250 h. This finding further demonstrates the advantage of the N–CN-Fd catalyst in increasing the discharge-charge capacity and improving the cycling stability of the Li–O_2 battery.

3.3. Theoretical investigation

According to XPS and IR characterization data, it is found that after freeze-drying, the content of electron-withdrawing C=O single bonds decreases whereas the content of electron-donating N–H bonds increase in the samples. Furthermore, a 3D AFM image of the N–CN-Fd displays a transparent and nearly monolayer structure. About the aperiodic and periodical structure, we consider the minimize the influence of the number of atoms or shape on the adsorption strength as much as possible. At the same time, there is no obvious difference between the two models of nanoribbons and cluster, which were tested and listed in Fig. S17. Therefore, we cautiously design various monolayer surface models (FeN_3-Graphene (FeN_3-G), Arm/Zig-Pyridinic N (Arm/Zig-PyN), Edge graphite N (EGN)/Graphite N (GN), Pyrrolic N, Amino N, and OH/COOH doped) to study the effects of different functional groups and N doped sites on the catalytic performance. The potential determining step (PDS) depended on the different adsorption strength of various oxygenated intermediates in the four-step ORR transfer pathway of O_2 to OH^- (Fig. 5a and Table S5). In comparison, the ΔG*OH vs ΔG*OOH of functional group doped graphene slab in Fig. S18 show very weak linear correlation, which is different from that Fe–N coordinate materials (Fig. S18). The strongest OH Gibbs adsorption energy is −1.47 eV (Amino N for −0.15 eV and Arm-PyN for 0.97 eV) for FeN_3-G, and the weakest OOH adsorption is 4.09 eV (FeN_3-G for 0.59 and Amino N for 2.96 eV) for Arm-PyN. According to the free energy diagram (Fig. S19), the surface reaction rate of other active sites is controlled by O_2 to OOH* except that FeN_3-G is OH* to OH^-. From Fig. 5b, we can also see that EGN lies closest to the top of the overpotential volcano, and the overpotential of EGN is 0.62 eV, which is lower than 1.01 eV for FeN_3-G and 1.79 eV for Arm-PyN. The overpotential order of active sites located at two ends of the volcano is COOH > FeN_3-G > Pyrrolic N > GN > Arm-PyN. Meanwhile, the overpotential order of active sites at the near top of the volcano is EGN > OH > Zig-PyN > Amino N, which reveals better reaction activity.

To investigate adsorbed sites in ORR, the calculated partial density of states (PDOS) of the carbon atom adsorbed intermediate products were shown in Fig. 5c. The best adsorption sites of intermediate species almost all located on ortho/sub-ortho carbon atoms sites except for that of the OH doped and FeN_3-G slabs (Fig. S20). The electronic states near the Fermi level of active carbon atoms in a variety of doped graphene materials are predominately contributed by the p_z orbital (Fig. 5c). In 2D graphene, p_x, and p_y orbitals in each carbon atom undergo sp^2 hybridization to form σ bonds with neighboring atoms along the horizontal lattice. Consequently, the p_z orbital in a carbon atom, perpendicular to the graphene plane, can participate in the bonding interaction with adsorbed molecules on the surface significantly. The higher density of p_z states further enhances the ability of perpendicular bonding interaction. Near the Fermi level, comparing with the pz orbit electron of Arm-PyN and GN, Zig-PyN and EGN has much more occupied. The linear relationship of p-band center and G_{OH*} about various graphene doping structures show that comparing with GN, Zig-PyN and EGN has more interaction strengths with intermediates (Fig. S21). Meanwhile, the difference charge in Fig. 5d demonstrates that the introduction of functional groups can effectively activate π-electrons, and for zig-PyN and amino N, the charge of adjacent carbon atoms increases by 0.15 e^- and 0.24 e^- respectively, while COOH doped only increases by 0.04 e^- and the phenomenon of edge functionalization has been confirmed by many reports [48,49]. Overall, the abundant electron-donating surface groups (E.G. Amino N and OH group) effectively activate the electronic structure of the ortho-C atom, thus enhancing the adsorption strength of the intermediate OOH (compare with GN and Arm-PyN), which endow the catalysts robust ORR activity.

4. Conclusions

In summary, a biomass carbon architecture, decorating the abundant electron-donating activate sites, is well-designed and synthesized via a low-cost and scalable freeze-drying technology. The growing electron-donating groups of N–CN-Fd through a freeze-drying process create incredible ORR catalytic activities and stability. The obtained N–CN-Fd displays an onset potential of 0.91 V, a half-wave potential of 0.79 V, and a limited-diffusion current density of 3.6 mA/cm^2 for ORR under alkaline conditions, comparable to commercial Pt/C (0.93 V, 0.82 V, and 5.00 mA/cm^2, respectively). The Koutecky-Levich equation and rotating ring-disk electrode tests reveal a four-electron ORR pathway, impeding hydrogen peroxide generation. Moreover, N–CN-Fd maintains higher stability than Pt/C in chronoamperometric response tests. Due to the outstanding activity of N–CN-Fd, the rechargeable Li–O_2 battery using N–CN-Fd as the cathode catalyst exhibits a high energy density, a low charge/discharge voltage gap, ultra-strong reversibility, and long cycling stability. First-principles simulations elucidated that the abundant electron-donating surface groups on the N–CN-Fd are crucial to generate robust ORR activity. The carbon atoms adjacent to electron-donating groups (such as OH and NH_2 group) act as the most active sites for the ORR, which very important to have reasonable adsorption of OOH on the surface. This scalability and low-cost electron-donating/electron-withdrawing groups engineering strategy are facilitated via a freeze-drying route for improving the catalytic performance, we expect this innovative methodology would pave a way to fabricate novel carbon-based nanomaterials, as a competitive candidate to replace Pt for ORR and Li–O_2 battery, which definitely could broaden electrochemical and catalytic applicability for producing

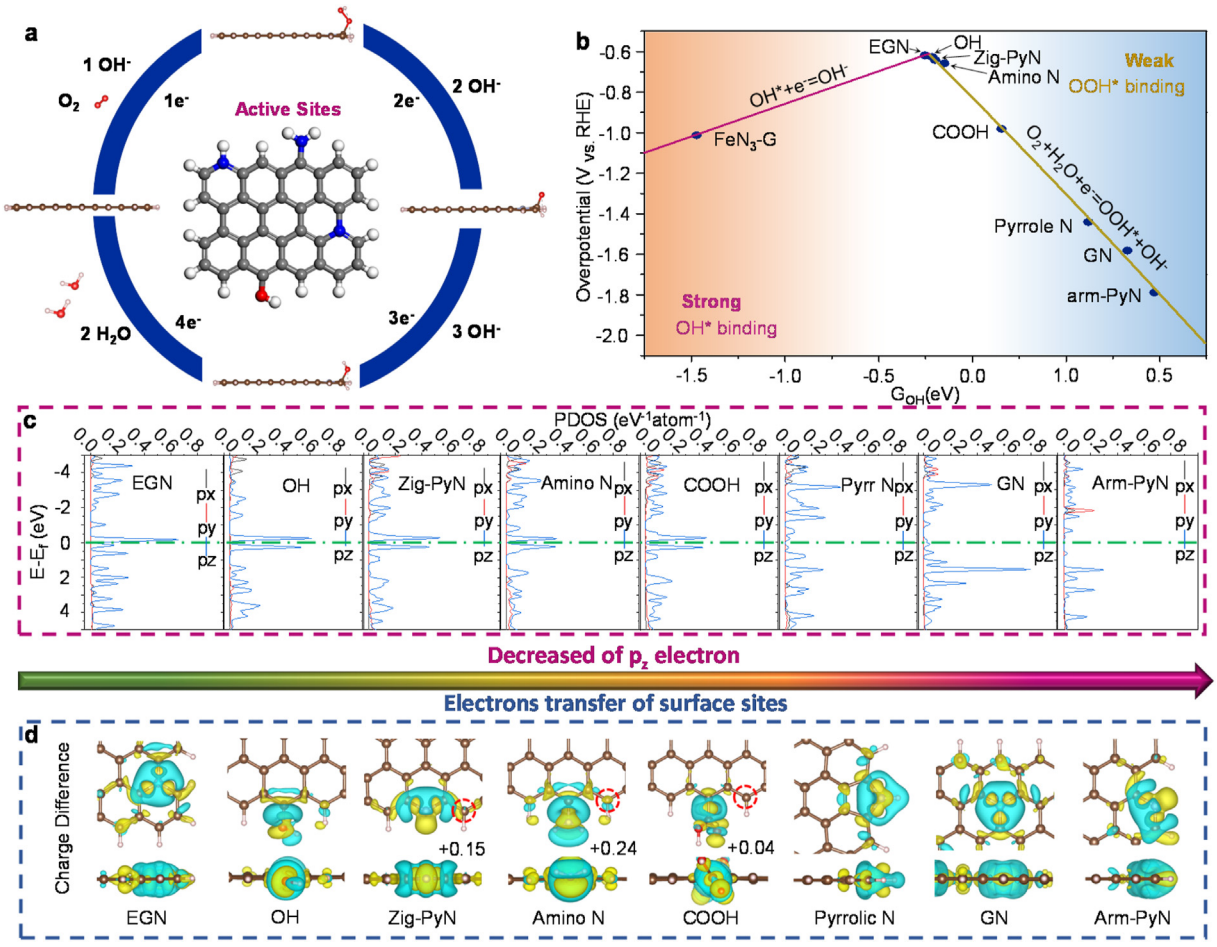

Fig. 5. (a) Illustration of the ORR base pathway on the EGN slab. (b) Volcano plot between ΔG_{*OH} and the ORR overpotential for doped graphene structures. (c) Calculated partial density of states (PDOS) of the carbon atom adsorbed various intermediate products. The Fermi level is shown as a green dashed line. (d) Top and side views of charge density difference mappings for various doping structures. Yellow: charge accumulation; cyan: charge depletion. The active carbon atom is marked with a red dashed circle. Isosurface level = 0.003 e/Bohr^3. $\Delta\rho = \rho$(slab + ads)-ρ(slab)-ρ(ads). Model scale: 1.5 nm. (A colour version of this figure can be viewed online.)

other carbon-based metal-free catalyst systems.

CRediT authorship contribution statement

Gao Li: Writing – original draft, Investigation. **Huanhuan Guo:** Writing – original draft, Investigation. **Zeming Wang:** Writing – original draft, Investigation. **Hong Bao:** Visualization, Investigation. **Guanhui Gao:** Visualization, Investigation. **Bingjie Hu:** Visualization, Investigation. **Lijie Ci:** Visualization, Investigation. **Liang Wang:** Supervision, Writing – review & editing, Investigation, Funding acquisition. **Minghong Wu:** Supervision, Investigation, Funding acquisition.

Declaration of competing interest

The authors declare that they have no known competing financial interests or personal relationships that could have appeared to influence the work reported in this paper.

Acknowledgements

The project was funded by National Natural Science Foundation of China (Nos. 21901154, 21671129), the Program for Changjiang Scholars and Innovative Research Team in University (No. IRT17R71). We thank the Laboratory for Microstructures of Shanghai University.

Appendix A. Supplementary data

Supplementary data to this article can be found online at https://doi.org/10.1016/j.carbon.2021.09.042.

References

[1] G. Centi, S. Perathoner, Towards solar fuels from water and CO_2, ChemSusChem 3 (2) (2010) 195–208.
[2] J.C. Li, X. Qin, F. Xiao, C. Liang, M. Xu, Y. Meng, E. Sarnello, L. Fang, T. Li, S. Ding, Z. Lyu, S. Zhu, X. Pan, P.X. Hou, C. Liu, Y. Lin, M. Shao, Highly dispersive cerium atoms on carbon nanowires as oxygen reduction reaction electrocatalysts for Zn–air batteries, Nano Lett. 21 (10) (2021) 4508–4515.
[3] W. Li, C. Han, K. Zhang, S. Chou, S. Dou, Strategies for boosting carbon electrocatalysts for the oxygen reduction reaction in non-aqueous metal–air battery systems, J. Mater. Chem. A. 9 (11) (2021) 6671–6693.
[4] M. Li, X. Bi, R. Wang, Y. Li, G. Jiang, L. Li, C. Zhong, Z. Chen, J. Lu, Relating catalysis between fuel cell and metal-air batteries, Matter 2 (1) (2020) 32–49.
[5] W. Zhu, H. Yuan, F. Liao, Y. Shen, H. Shi, Y. Shi, L. Xu, M. Ma, M. Shao, Strain engineering for Janus palladium-gold bimetallic nanoparticles: enhanced electrocatalytic performance for oxygen reduction reaction and zinc-air battery, Chem. Eng. J. 389 (2020) 124240.
[6] H.B. Yang, J. Miao, S.F. Hung, J. Chen, H.B. Tao, X. Wang, L. Zhang, R. Chen, J. Gao, H. Chen, M.L. Dai, B. Liu, Identification of catalytic sites for oxygen reduction and oxygen evolution in N-doped graphene materials: development of highly efficient metal-free bifunctional electrocatalyst, Sci. Adv. 2 (4) (2016), e1501122.
[7] M. Piana, S. Catanorchi, H.A. Gasteiger, Kinetics of non-platinum group metal

catalysts for the oxygen reduction reaction in alkaline medium, ECS Trans 16 (2) (2008) 2045–2055.
[8] Q. Lai, J. Zheng, Z. Tang, D. Bi, J. Zhao, Y. Liang, Optimal configuration of N-doped carbon defects in 2D turbostratic carbon nanomesh for advanced oxygen reduction electrocatalysis, Angew. Chem. Int. Ed. 59 (29) (2020) 2–10.
[9] D. Gu, F. Wang, K. Yan, R. Ma, J.A. Wang, Thermally decomposable template route to synthesize nitrogen-doped wrinkled carbon nanosheets as highly efficient and stable electrocatalysts for the oxygen reduction reaction, ACS Sustain. Chem. Eng. 6 (2) (2017) 1951–1960.
[10] J. Duan, S. Chen, M. Jaroniec, S.Z. Qiao, Heteroatom-doped graphene-based materials for energy-relevant electrocatalytic processes, ACS Catal. 5 (9) (2015) 5207–5234.
[11] D. Gu, R. Ma, Y. Zhou, F. Wang, K. Yan, Q. Liu, J. Wang, Synthesis of nitrogen-doped porous carbon spheres with improved porosity toward the electrocatalytic oxygen reduction, ACS Sustain. Chem. Eng. 5 (11) (2017) 11105–11116.
[12] C. Zhu, H. Li, S. Fu, D. Du, Y. Lin, Highly efficient nonprecious metal catalysts towards oxygen reduction reaction based on three-dimensional porous carbon nanostructures, Chem. Soc. Rev. 45 (3) (2016) 517–531.
[13] Z.P. Zhang, X.J. Gao, M.L. Dou, J. Ji, F. Wang, Biomass derived N-doped porous carbon supported single Fe atoms as superior electrocatalysts for oxygen reduction, Small 13 (22) (2017) 1604290.
[14] Q.L. Zhu, W. Xia, L.R. Zheng, R. Zou, Z. Liu, Q. Xu, Atomically dispersed Fe/N-doped hierarchical carbon architectures derived from a metal-organic framework composite for extremely efficient electrocatalysis, ACS Energy Lett 2 (2) (2017) 504–511.
[15] B. Zhang, Y. Liu, M. Ren, W. Li, X. Zhang, R. Vajtai, P.M. Ajayan, J.M. Tour, L. Wang, Sustainable synthesis of bright green fluorescent nitrogen-doped carbon quantum dots from alkali lignin, ChemSusChem 12 (18) (2019) 4202–4210.
[16] C. Hu, L. Dai, Carbon-based metal-free catalysts for electrocatalysis beyond the ORR, Angew. Chem. Int. Ed. 55 (2) (2016) 11736–11758.
[17] Y. Wang, C. Xie, Z. Zhang, D. Liu, R. Chen, S. Wang, In situ exfoliated, N-doped, and edge-rich ultrathin layered double hydroxides nanosheets for oxygen evolution reaction, Adv. Funct. Mater. 28 (4) (2018) 1703363.
[18] X.H. Li, M. Antonietti, Polycondensation of boron- and nitrogen-codoped holey graphene monoliths from molecules: carbocatalysts for selective oxidation, Angew. Chem. Int. Ed. 52 (17) (2013) 4572–4576.
[19] J.P. Paraknowitsch, A. Thomas, Doping carbons beyond nitrogen: an overview of advanced heteroatom doped carbons with boron, sulphur and phosphorus for energy applications, Energy Environ. Sci. 6 (10) (2013) 2839.
[20] X. Wang, G. Sun, R.P. outh, D.H. Kim, W. Huang, P. Chen, Heteroatom-doped graphene materials: syntheses, properties and applications, Chem. Soc. Rev. 43 (20) (2014) 7067–7098.
[21] Y. Li, Z.Y. Fu, B.L. Su, Hierarchically structured porous materials for energy conversion and storage, Adv. Funct. Mater. 22 (22) (2012) 4634–4667.
[22] H. Wang, Y. Shao, S. Mei, Y. Lu, M. Zhang, J.K. Sun, K. Matyjaszewski, M. Antonietti, J. Yuan, Polymer-derived heteroatom-doped porous carbon materials, Chem. Rev. 120 (17) (2020) 9363–9419.
[23] Z. Zhang, S. Yang, H. Li, Y. Zan, X. Li, Y. Zhu, M. Dou, F. Wang, Sustainable carbonaceous materials derived from biomass as metal-free electrocatalysts, Adv. Mater. 31 (13) (2018) 1805718.
[24] Q. Li, T. He, Y.Q. Zhang, H. Wu, J. Liu, Y. Qi, Y. Lei, H. Chen, Z. Sun, C. Peng, L. Yi, Y. Zhang, Biomass waste-derived 3d metal-free porous carbon as a bifunctional electrocatalyst for rechargeable zinc-air batteries, ACS Sustain. Chem. Eng. 7 (20) (2019) 17039–17046.
[25] X. Shen, G. Yu, Z. Zhang, J. Liu, H. Li, X. Huang, W. Chen, Covalent surface modification with electron-donating/accepting π-conjugated chains to effectively tune the electronic and magnetic properties of zigzag SiC nanoribbons, J. Mater. Chem. C 5 (8) (2017) 2022–2032.
[26] N. Ramaswamy, U. Tylus, Q. Jia, S. Mukerjee, Activity descriptor identification for oxygen reduction on nonprecious electrocatalysts: linking surface science to coordination chemistry, J. Am. Chem. Soc. 135 (41) (2013) 15443–15449.
[27] G. Zhou, Y. Ma, X. Wu, Y. Lin, H. Pang, M. Zhang, L. Xu, Z. Tian, Y. Tang, Electronic modulation by N incorporation boosts the electrocatalytic performance of urchin-like Ni_5P_4 hollow microspheres for hydrogen evolution, Chem. Eng. J. 402 (2020) 126302.
[28] X.H. Liu, J.J. Kang, Y. Dai, C.C. Dong, X.H. Guo, X. Jia, Graphene-like nitrogen-doped carbon nanosheet prepared from direct calcination of dopamine confined by g-C_3N_4 for oxygen reduction, Adv. Mater. Interfaces 5 (14) (2018) 1800303.
[29] C. Wang, N.H. Xie, Y. Zhang, Z. Huang, K. Xia, H. Wang, S. Guo, B.Q. Xu, Y. Zhang, Silk-derived highly active oxygen electrocatalysts for flexible and rechargeable Zn-air batteries, Chem. Mater. 31 (3) (2019) 1023–1029.
[30] Y. Tan, C. Xu, G. Chen, X. Fang, N. Zheng, Q. Xie, Facile synthesis of manganese-oxide-containing mesoporous nitrogen-doped carbon for efficient oxygen reduction, Adv. Funct. Mater. 22 (21) (2012) 4584–4591.
[31] G. Kresse, J. Furthmuller, Efficient iterative schemes for ab initio total-energy calculations using a plane-wave basis set, Phys. Rev. B 54 (16) (1996) 11169–11186.
[32] G. Kresse, D. Joubert, From ultrasoft pseudopotentials to the projector augmented-wave method, Phys. Rev. B 59 (3) (1999) 1758–1775.
[33] John P. Perdew, J.A. Chevary, S.H. Vosko, Koblar A. Jackson, Mark R. Pederson, D.J. Singh, Carlos Fiolhais, Atoms, molecules, solids, and surfaces applications of the generalized gradient approximation for exchange and correlation, Phys. Rev. B 46 (11) (1992) 6671–6687.
[34] H.J. Monkhorst, J.D. Pack, Special points for brillouin-zone integrations, Phys. Rev. B 13 (1976) 5188–5192.
[35] K. Mathew, R. Sundararaman, K. Letchworth-Weaver, T.A. Arias, R.G. Hennig, Implicit solvation model for density-functional study of nanocrystal surfaces and reaction pathways, J. Chem. Phys. 140 (8) (2014), 084106.
[36] K. Mathew, V. Kolluru, S. Mula, S. Steinmann, R. Hennig, Implicit self-consistent electrolyte model in plane-wave density-functional theory, J. Chem. Phys. 151 (2019) 234101–234108.
[37] D.S. Yang, D. Bhattacharjya, S. Inamdar, J. Park, J.S. Yu, Phosphorus-doped ordered mesoporous carbons with different lengths as efficient metal-free electrocatalysts for oxygen reduction reaction in alkaline media, J. Am. Chem. Soc. 134 (39) (2012) 16127–16130.
[38] S. Yang, X. Feng, X. Wang, K. Mullen, Graphene-based carbon nitride nanosheets as efficient metal-free electrocatalysts for oxygen reduction reactions, Angew. Chem. Int. Ed. 50 (23) (2011) 5339–5343.
[39] B. Zhang, C. Wang, D. Liu, Y. Liu, X. Yu, L. Wang, Boosting ORR electrocatalytic performance of metal-free mesoporous biomass carbon by synergism of huge specific surface area and ultrahigh pyridinic nitrogen doping, ACS Sustain. Chem. Eng. 6 (11) (2018) 13807–13812.
[40] R. Zhou, Y. Zheng, M. Jaroniec, S.Z. Qiao, Determination of the electron transfer number for the oxygen reduction reaction: from theory to experiment, ACS Catal. 6 (7) (2016) 4720–4728.
[41] R. Liu, D. Wu, X. Feng, K. Mullen, Nitrogen-doped ordered mesoporous graphitic arrays with high electrocatalytic activity for oxygen reduction, Angew. Chem. Int. Ed. 49 (14) (2010) 2565–2569.
[42] Y. Zheng, Y. Jiao, L. Ge, M. Jaroniec, S.Z. Qiao, Two-step boron and nitrogen doping in graphene for enhanced synergistic catalysis, Angew. Chem. Int. Ed. 52 (11) (2013) 3110–3116.
[43] M. Borghei, J. Lehtonen, L. Liu, O.J. Rojas, Advanced biomass-derived electrocatalysts for the oxygen reduction reaction, Adv. Mater. 30 (24) (2018), e1703691.
[44] S.L. Zhao, H.J. Yin, L. Du, L.C. He, K. Zhao, L. Chang, G.P. Yin, H.J. Zhao, S.Q. Liu, Z.Y. Tang, Carbonized nanoscale metal-organic frameworks as high performance electrocatalyst for oxygen reduction reaction, ACS Nano 8 (12) (2014) 12660.
[45] E.M. Miner, M. Dincă, Metal-organic frameworks: evolved oxygen evolution catalysts, Nat. Energy 1 (12) (2016) 16186.
[46] J.Q. Sun, H.J. Yin, P.R. Liu, Y. Wang, X.D. Yao, Z.Y. Tang, H.J. Zhao, Molecular engineering of Ni-/Co-porphyrin multilayers on reduced graphene oxide sheets as bifunctional catalysts for oxygen evolution and oxygen reduction reactions, Chem. Sci. 7 (9) (2016) 5640.
[47] J.K. Nørskov, J. Rossmeisl, A. Logadottir, L. Lindqvist, Origin of the overpotential for oxygen reduction at a fuel-cell cathode, J. Phys. Chem. B 108 (46) (2004) 17886–17892.
[48] S. Yang, Y. Yu, M. Dou, Z. Zhang, F. Wang, Edge-functionalized polyphthalocyanine networks with high oxygen reduction reaction Activity, J. Am. Chem. Soc. 142 (41) (2020) 17524–17530.
[49] X. Zou, L. Wang, B.I. Yakobson, Mechanisms of the oxygen reduction reaction on B- and or N-doped carbon nanomaterials with curvature and edge effects, Nanoscale 10 (3) (2018) 1129–1134.